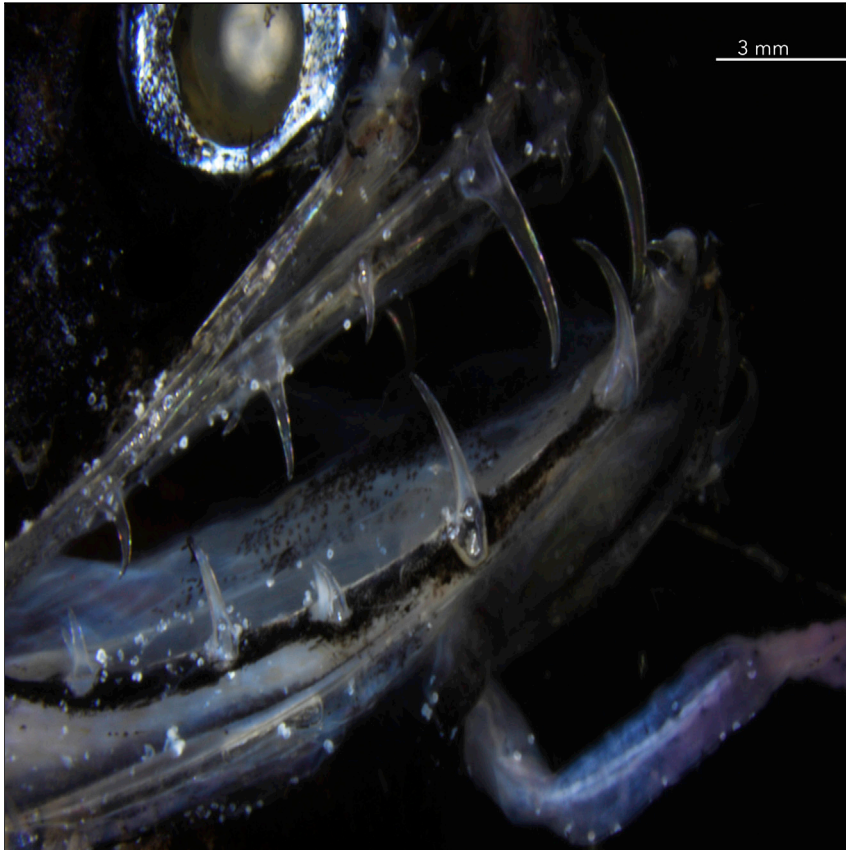


## Article

# On the Nature of the Transparent Teeth of the Deep-Sea Dragonfish, *Aristostomias scintillans*



Audrey Velasco-Hogan, Dimitri D. Deheyn, Marcus Koch, Birgit Nothdurft, Eduard Arzt, Marc A. Meyers

mameyers@ucsd.edu

## HIGHLIGHTS

The transparent teeth are nanostructured, resulting in reduced Rayleigh scattering

This camouflages the fish's open mouth in the darkness of the deep ocean

The teeth are found to have a gradient in mineralization

Teeth lack microscale features, such as dentin tubules, which reduce scattering

Deep-sea fishes living in darkness have evolved unique predation and communication mechanisms involving bioluminescence and other stratagems. Another adaptation is the transparency of the teeth of several species, which is hypothesized to provide stealth for predation. We investigated the transparent teeth of the dragonfish and discovered that it is due to the mixture of nanocrystalline and amorphous phases in both its enamel-like and dentin layers and the absence of tubules. This structure significantly decreases the Rayleigh scattering of the hydroxyapatite-collagen mixture.



## Benchmark

First qualification/assessment of material properties and/or performance

Velasco-Hogan et al., Matter 1, 235–249  
July 10, 2019 © 2019 Elsevier Inc.  
<https://doi.org/10.1016/j.matt.2019.05.010>



## Article

# On the Nature of the Transparent Teeth of the Deep-Sea Dragonfish, *Aristostomias scintillans*

Audrey Velasco-Hogan,<sup>1</sup> Dimitri D. Deheyn,<sup>2</sup> Marcus Koch,<sup>3</sup> Birgit Nothdurft,<sup>3</sup> Eduard Arzt,<sup>3,4</sup> and Marc A. Meyers<sup>1,5,\*</sup>

## SUMMARY

The dragonfish is a voracious predator of the deep sea with an arsenal of tools to hunt prey and remain concealed. In contrast to its dark pigmented skin, the dragonfish is equipped with transparent teeth. Here, we establish the structure, composition, and mechanical properties of the transparent teeth for the first time. We find the enamel-like layer to consist of nanocrystalline hydroxyapatite domains (~20 nm grain size) embedded in an amorphous matrix, whereas in the dentin layer the nanocrystalline hydroxyapatite coats nanoscale collagen fibrils forming nanorods. This nanoscale structure is responsible for the much-reduced Rayleigh light scattering, which is further ensured by the sufficiently thin walls. Here, we suggest that the nanostructured design of the transparent dragonfish teeth enables predatory success as it makes its wide-open mouth armed with saber-like teeth effectively disappear, showing no contrast to the surrounding blackness of the fish nor the background darkness of the deep sea.

## INTRODUCTION

Despite the recent abundance of research on biological materials,<sup>1–4</sup> including those of marine origin,<sup>5</sup> organisms that live at great ocean depths have been virtually unexplored, both in terms of their structure-property relationships and potential for bioinspiration. This is in no small part due to the difficulty in accessing these pelagic depths (down to 4,000 m on average) and extracting specimens for study. The physics driving the biology of deep-sea animals (and therefore the biological materials they make) is indeed complex, and still poorly understood with regard to its regulatory effects on biological processes. To predict some of the “deep-sea effects” on biological materials, one must note a number of unique features characteristic of deep-sea environments: lack of ambient light,<sup>6</sup> low temperatures, and high pressures.<sup>7,8</sup> As a result of these extreme conditions, fascinating adaptations have evolved.

A unique observation is that the teeth of several deep-sea fishes are rather transparent. These teeth have heretofore not been studied, and until now their structure, mechanical properties, and ecological function have remained unreported. Herein, we show that the teeth are composed of two homogeneous concentric layers, namely enamel-like and dentin, which constitute the wall of the teeth, and that they are nanostructured, resulting in reduced Rayleigh scattering of light.

## Progress and Potential

This study opens the door to further investigation into teeth of deep-sea fish. The methodology developed can be applied to other species.



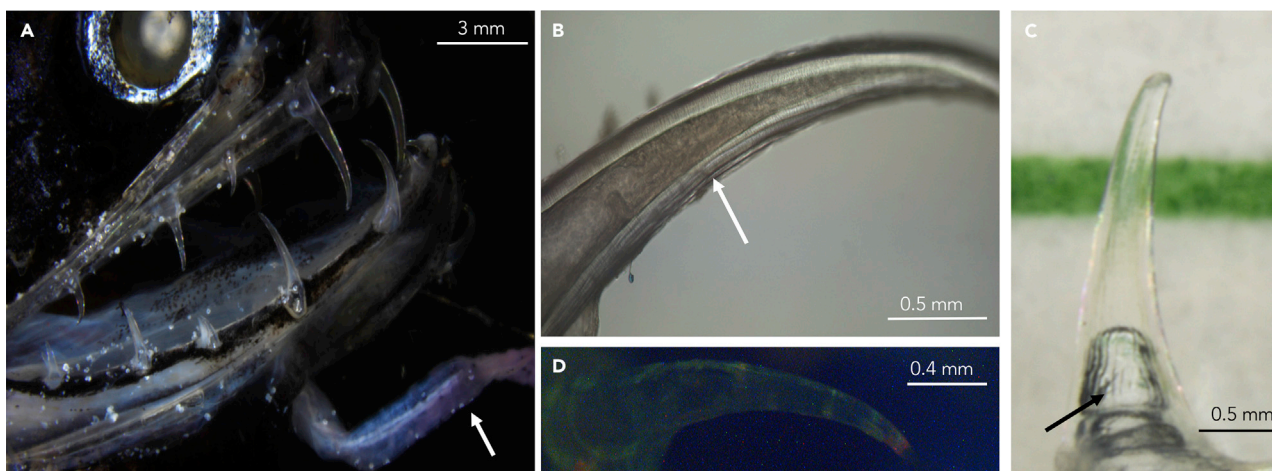


**Figure 1. Light Microscopy of Dragonfish Teeth**

(A) Head of a freshly collected specimen showing the row of teeth erecting outward from the jaw. Arrow points to the barbel. Image taken of the head in filtered seawater and captured using a polarizing filter.

(B) Close-up, showing optical evidence of concentric layers and hollowness of the tooth. Image taken in filtered seawater with an immersive lens. Arrow points to the striations seen on the concave side.

(C) Tooth imaged in seawater with color line behind to demonstrate transparency. The arrow indicates an air bubble within the hollow cavity of the tooth due to dissection from the jaw. Image captured with a polarizing filter.

(D) Tooth under fluorescence excited at a broadband excitation 440–490 nm and collected with a long-pass filter (>515 nm). This image shows little fluorescence. Image taken of a dry specimen in air.

## RESULTS AND DISCUSSION

### Optical Performance in Transmittance and Reflectance

Deep-sea dragonfish, belonging to the family Stomiidae, are apex predators that typically feed on smaller myctophiform and gonostomatid fishes.<sup>9,10</sup> Thus, they have proportionately enormous jaws capable of a special mechanism of opening and closure referred to as “loosejaw.” This mechanism allows the dragonfish to open its jaw to a greater extent than a conventional jaw of similar size, and enables it to ingest preys up to 50% of its own size.<sup>11</sup> This design allows for effective predation as the dragonfish can ingest large prey for sustained energy, which are often scarce in the deep sea. It has also been reported that the jaw muscles of the dragonfish are weak<sup>11</sup> and therefore that the large fangs must be sharp, as confirmed by their slim and pointed outline (Figure 1), to pierce prey effectively. These teeth, although “large” relative to the jaw, and in fact sticking out of it in many cases, are difficult to see because they range from translucent to transparent for light depending on whether in air or water, respectively.

In terms of spectral translucency, the teeth analyzed in filtered seawater showed light transmittance that changed gradually with the color spectrum, increasing gradually from ~38% in the blue range to ~73% of light in the red range (Figure 2B). This is a significant increase of transmittance when compared with analysis done in air, which showed transmittance around ~32% of light in the blue range to ~35% of transmittance in the green-red range (Figure S1). Although a limited amount of this difference could come from technical challenges of capturing light transmittance in water rather than air, the difference is likely to originate mainly from differences of refractive indices between the inside of the tooth material and the outside medium (water versus air). In water, the interfaces with the tooth material show a smaller difference of refractive index than for air, causing light to be less diffracted sideways when penetrating and existing the tooth, resulting in it becoming more transparent than

<sup>1</sup>Materials Science and Engineering Program, University of California, San Diego, USA

<sup>2</sup>Scripps Institution of Oceanography, University of California, San Diego, USA

<sup>3</sup>INM - Leibniz Institute for New Materials, Saarbrücken, Germany

<sup>4</sup>Saarland University, Saarbrücken, Germany

<sup>5</sup>Lead Contact

\*Correspondence: [mameyers@ucsd.edu](mailto:mameyers@ucsd.edu)

<https://doi.org/10.1016/j.matt.2019.05.010>

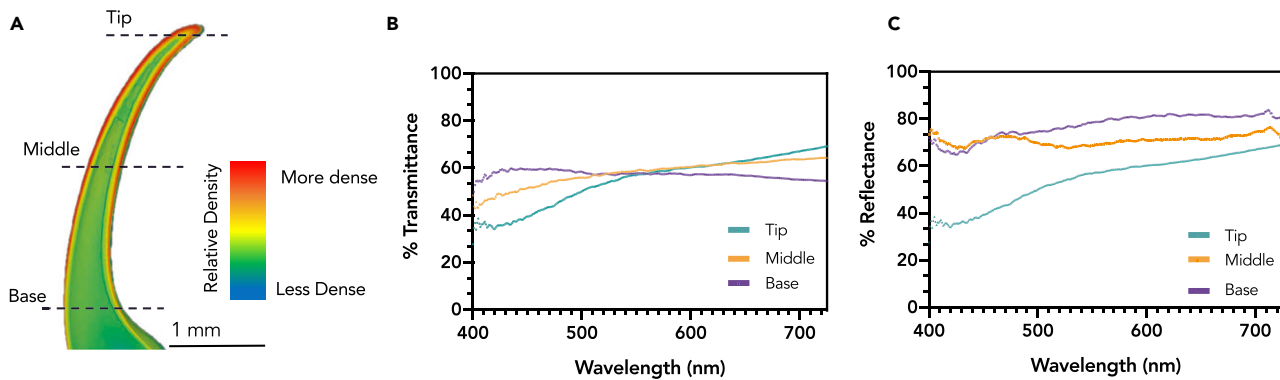


**Figure 2. Optical Properties in Transmittance and Reflectance**

(A)  $\mu$ -CT scan of a longitudinal cross-section of a representative tooth. The color mapping indicates relative density signifying degree of mineralization. Hotter colors (red) are more dense while cooler colors (blue) are less dense. Dashed lines represent relative locations where analysis was performed. (B) Transmittance for three sections of one tooth (tip, middle, base) with respect to wavelength. (C) Reflectance for three sections (tip, middle, base) with respect to wavelength. See also Figure S1.

in air. To analyze the effect of tooth material (tooth thickness and relative mineralized density) on the transparency, we performed hyperspectral analysis at three different locations along the tooth (tip, middle, base) considering that the micro-computed tomography ( $\mu$ -CT) data (Figure 2A) clearly showed a gradient structure along the length of the tooth. The base is thicker and less mineralized (indicated by the cooler colors) while the tip is thinner and more mineralized (indicated by the hotter colors). The tip transmits less light in the blue range and more light in the red range when compared with the base and middle sections. As expected, all sections of the tooth transmit less light in the blue range, which is due to an increase in Rayleigh scattering that is inversely proportional to the fourth power of wavelength.

The transparency of the teeth of the deep-sea dragonfish *Aristostomias scintillans*, in terms of both level of transparency and spectral difference, is comparable with that of the shell of the shallow-water oyster *Placuna placenta*. In this shell, transmittance ranges from  $\sim$ 20% in the blue range up to  $\sim$ 80% in the red range, which is homogeneous spatially for various thicknesses (71–660  $\mu$ m).<sup>12</sup> *P. placenta* is a shallow-water oyster. Transparency in shallow waters where sunlight is abundant is critical for camouflage but also for sunlight to reach photosymbionts that could live under shell structures.<sup>13</sup> At such great depths where the dragonfish is found, there is only light from bioluminescence, which causes the effectiveness for transparency to increase dramatically.<sup>14</sup> For example, the contrast threshold for a cod's eye increases from 0.02 at light intensities found at 200 m to 0.5 at 650 m, where it would be unable to detect tissues with a transparency greater than 50%.<sup>14</sup> This suggests that the transparent teeth, while comparable with a shallow-water oyster, are much more effective in the greater depths of the ocean.

While transmittance is an indicator of transparency by measurement of how much light can pass through a material without being lost (e.g., via scattering, absorbance), it is also valuable to analyze reflectance. Reflectance is important from an ecological standpoint as it signifies the amount of light that would shine back from the tooth surface and can therefore illuminate the fish's presence. Reflectance was analyzed with hyperspectral imaging at three positions similar to those for transmittance (tip, middle, base) to differentiate between structural effects along the tooth. The teeth were analyzed against a white background, and since they are

translucent the background influences the reflectance. Reflectance near 100% indicates how closely matched to the background the material is (i.e., the more transparent it is). Anything less than 100% reflectance suggests that the light was lost due to various mechanisms such as scattering and absorbance. The teeth analyzed showed reflectance in filtered seawater from 39% of light in the blue range to 86% of light in the red range (Figure 2C). The base of the tooth had the greatest reflectance of 70% in the blue range and 86% in the red range. Again, reflectance in the blue range was decreased due to an increase in Rayleigh scattering for blue light. The reflectance analysis shows that the teeth match fairly well to the white background and therefore are not likely to reveal the presence of the dragonfish to either prey or predator.

We believe that the elaborate structural arrangement of the teeth, which provides mechanical strength combined with transparency, enhances predatory performance of the fish. The dragonfish is indeed a top predator of the deep sea, with a dark sleek body that is equipped with rows of photophores<sup>15</sup> along the ventral region and a light-producing barbel attached to its chin.<sup>16</sup> The ventral photophores' light emission matches that of downwelling environmental light camouflaging its silhouette.<sup>15</sup> While the barbel is used to attract the attention of its prey, the dragonfish body and mouth in particular must remain hidden for effective hunting.<sup>16,17</sup> We suggest that the transparent teeth provide an additional successful camouflage strategy by reducing the scattering of light (from any possible bioluminescence from the dragonfish itself and/or its possible prey) and being therefore concealed against the darkness of the mouth and/or deep ocean.

### Structural Characterization of Enamel-like and Dentin Layers

Under white-light illumination, it was detected that the teeth have two types of surfaces: smooth and striated (Figures 1B, S2, and S3). The rough surface is located mainly on the concave section of the tooth and consists of longitudinal striations and ridges. The smooth surface is located elsewhere on the tooth, which is thus characterized by an absence of significant surface features. All observed teeth have longitudinally aligned ridges on the concave surface, which are shown for eight representative teeth in Figure S3; these correspond to teeth imaged from the maxilla shown in Figure S2. The ridges are spaced  $\sim 20 \mu\text{m}$ , are sharp (radius at the tip  $\sim 1\text{--}2 \mu\text{m}$ ) and can effectively cut tissue. Some of the teeth show perforations at the base, which can act to increase their flexibility as the prey might be wiggling when caught (Figure S3).<sup>18</sup>

The teeth were observed under electron microscopy to obtain their principal morphometry, nanoscale structure, and composition. Overall, all teeth were found to have radii of curvature at the tip ranging from 2.5 to 5  $\mu\text{m}$ . This is extremely sharp when compared with piranha teeth<sup>19</sup> that have a radius of  $\sim 14 \mu\text{m}$  and the sharpest knives that have a radius of  $\sim 1 \mu\text{m}$ .<sup>20</sup> A notable number of teeth have significant wear and tip fractures, revealing the pulp cavity as shown in Figure 3. The fracture surface in Figures 3C and 3D highlights two subsurface layers: a smooth, apparently more brittle layer  $\sim 3 \mu\text{m}$  thick (marked 1) and a rougher layer (marked 2).

The features in the fracture surface align with the longitudinal tooth direction (Figures 3A and 3B). The surface of the tooth also exhibits a pattern of circumferential cracks that do not extend through the entire thickness but are restricted to the outside layer. This pattern of cracks is evidently produced by flexure of the tooth, which eventually led to its intentional fracture for observation (Figure S4A). The dentin layer, as will be seen later, has a structure that can provide greater toughness.

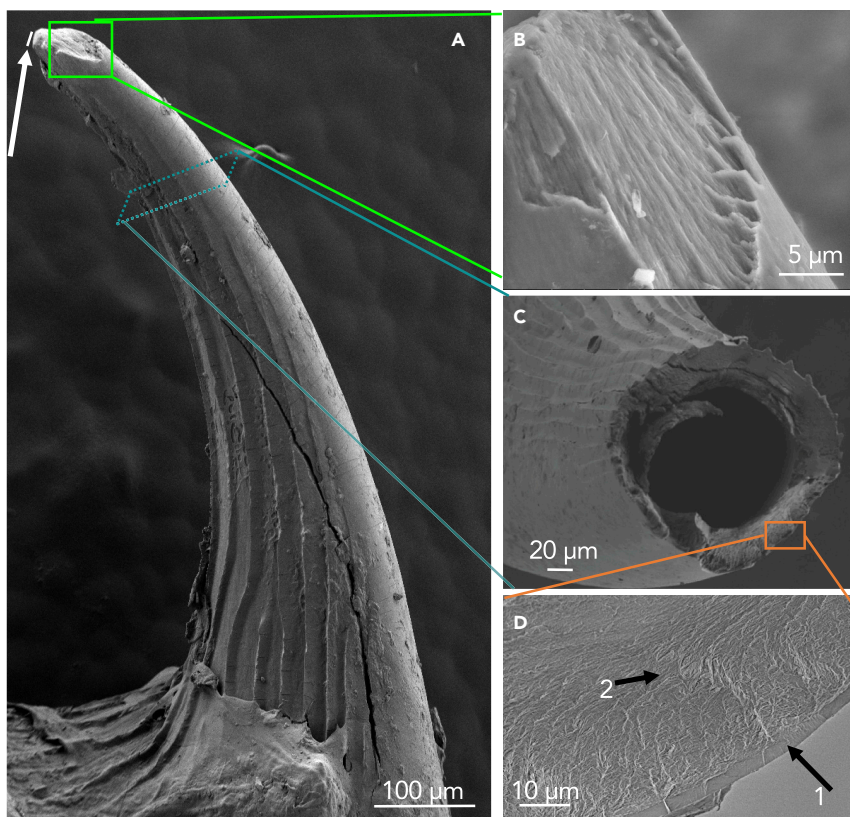


**Figure 3. Characteristic Teeth Exhibiting Longitudinal Striations on Concave Side**

(A) Shorter tooth from lower jaw with broken/worn tip. Arrow indicates radius of curvature.  
 (B) Surface wear near the tip of the tooth revealing the thin enamel-like surface and dentin layer, which has preferred orientation in the longitudinal direction.  
 (C) Transverse section showing detail of hollow pulp cavity.  
 (D) Enhanced transverse cross-section showing enamel-like outer layer ( $\sim 3 \mu\text{m}$ , marked 1) with smooth fracture surface and dentin (marked 2) with an irregular surface.

A specimen for transmission electron microscopy (TEM) was extracted by focused ion beam (FIB), and showed that cracks initiating at the surface arrest before reaching the dentin-enamel junction (Figure S4B).

Atomic-resolution TEM on specimens that were further thinned to  $\sim 40 \text{ nm}$  shows the characteristics of both the enamel-like and dentin layers (Figure 4A). The enamel-like layer consists of individual crystallites (Figure 4B) which, upon stacking, form Moiré patterns. The edges of the crystals are rounded, supporting the hypothesis that they are embedded in an amorphous matrix. The diffraction pattern (Figure 4C) exhibits a clear circular pattern (with individual spots embedded in the circle) and circular segments. One can distinguish a preferential orientation from the segments, and the diffraction pattern is similar to the one observed by Mahamid et al. (Figures 3B and 3C),<sup>21</sup> which they describe as poorly crystalline and clearly crystalline, respectively. The diameters of the rings coincide with those of Mahamid et al.<sup>21</sup> (002) and (004) (Table 1). A simple manner to interpret the structure is to consider it as a mixture of amorphous and nanocrystalline phases. The crystals have approximate dimensions of  $5 \times 20 \text{ nm}$ . They are difficult to resolve because their size is significantly smaller than the thickness of the foil ( $\sim 80 \text{ nm}$ ). However, additional characterization on a specimen subjected to a different preparation procedure

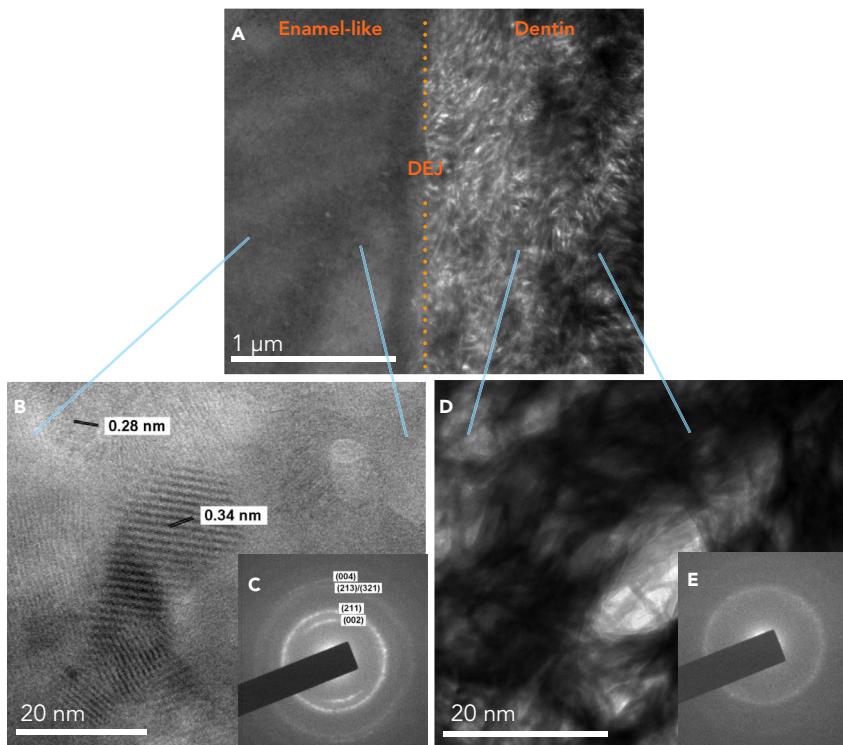


**Figure 4. TEM of the Nanostructured Enamel-like and Dentin Layers**

- (A) TEM showing the dentin-enamel-like junction (DEJ).  
 (B) TEM showing organized structuring of the enamel-like layer.  
 (C) Diffraction pattern of the enamel-like layer showing discrete spot characteristics of nanocrystalline structure and an amorphous structure (indicative of the diffuse background).  
 (D) TEM showing dentin consisting of a woven pattern of nanometer rods (~5 nm diameter).  
 (E) Diffraction pattern of dentin which shows greater amorphous characteristics than the enamel-like layer.

(detailed in [Supplemental Information](#)) confirmed the nanoscale features and Moiré pattern formation (Figure S5).

The dentin structure (Figures 4A and 4D) consists of nanometer-size rods (~5 nm diameter) forming an interwoven pattern by virtue of their “curvy” nature. There is also a degree of nanoscale porosity in the structure suggested by the spatial variation in electron transmission (darker and brighter regions adjoining each other). The diffraction pattern (Figure 4E) is more representative of an amorphous structure when compared with the enamel-like layer, which has clear diffraction spots embedded in the rings. The diffraction pattern shows a spacing of ~0.8 nm, which suggests that these are the (001) planes of hydroxyapatite (Table 1).

### Dentition Is Composed of Nanocrystalline Hydroxyapatite and Collagen

To determine the mineral nature, we first observed the teeth under blue-light illumination for fluorescence detection. Teeth of mammalian organisms fluoresce in the green when excited in UV light (350–400 nm). Such fluorescence has been extensively reported<sup>22</sup> and attributed not only to the organic matrix (collagen) of the teeth<sup>23,24</sup> but also to the mineral itself (dentin, enamel, and/or aragonite<sup>25–27</sup>). In the case of the dragonfish teeth, only limited fluorescence was observed when excited at 355 and 390 nm (Figures 1D and 1E). This indicates that the teeth are

**Table 1. Identification of Lattice Spacings from Diffraction Rings and Comparison**

Diffraction Files Ca <sub>5</sub> (PO <sub>4</sub> ) <sub>3</sub> (OH)	Intensity/Spacing (nm) from de Wolff <sup>28</sup>	Enamel-like (nm)	Dentin (nm)
(100)	12/0.817		
(002)	40/0.344	0.34	
(211)	100/0.281	0.27	0.28
(112)	60/0.278		
(300)	60/0.272		
(400)	12/0.1721	0.171	
(213)	40/0.184		0.18

not made of a brightly fluorescent mineral such as aragonite, and that any organic material is poor in aromatic amino acid known to have fluorescence, such as tryptophan, tyrosine, and histidine.

The diffraction patterns of the teeth allow for the identification of hydroxyapatite (HAP) Ca<sub>5</sub>(PO<sub>4</sub>)<sub>3</sub>(OH), as predicted. Table 1 provides the spacings and intensities, in the enamel-like and dentin layers, of the diffraction patterns.<sup>28</sup> Bright-field and dark-field TEM were used to determine the respective location of organic and inorganic material. As shown in Figure 5B, the dark-field micrograph highlights the individual nanorods, which are primarily composed of inorganic material. This suggests that the crystalline inorganic material is HAP, which is embedded within an organic matrix further characterized as collagen. The formation of HAP nanorods suggests preferential nucleation on collagen fibrils with diameters in the 5- to 10-nm range.

The presence of carbon in several of the quantitative scans (Figure S5) indicates collagen. This is confirmed using Fourier transform infrared spectroscopy (FTIR), which illustrates the intensity of functional groups detected by changes in dipole moment during molecular vibration. The functional groups that reveal the presence of collagen are the amide I, II, and III bands, which occur at 1,632, 1,536, and 1,240 cm<sup>-1</sup>, respectively (Figure 6 and Table S1).<sup>29,30</sup> Additionally, FTIR validates the presence of HAP with intensity bands corresponding to  $\nu_4\text{PO}_4^{3-}$ ,  $\nu_2\text{CO}_3^{2-}$ ,  $\nu_3\text{PO}_4^{3-}$ , and  $\nu_3\text{CO}_3^{2-}$  at 554 and 600, 870, 1,024, 1,410 cm<sup>-1</sup>, respectively (Figure 6 and Table S1).<sup>31</sup>

### Nanoscale Features Responsible for Reduced Rayleigh Scattering

Rayleigh scattering is a well-known phenomenon with a characteristic particle-size dependence. Rayleigh scattering applies to particles that are much smaller than the interacting wavelength of light satisfying the condition  $x \ll 1$  where  $x = 2\pi r/\lambda$ ,  $r$  is the radius of the particle, and  $\lambda$  is the wavelength of light. Rayleigh scattering numerical solutions work best for idealized systems of homogeneous spherical particles. This makes it difficult to apply to the system of the transparent teeth where the main constituent is randomly oriented nanorods. Scattering is highly dependent on particle size and orientation; therefore, spherical approximations are not sufficient for analyzing nanorods.<sup>32</sup>

For this reason, the Rayleigh-Gans-Debye approximation (RGD) is used for randomly oriented nanorods. Along with the conditions for Rayleigh scattering, RGD particles must be optically soft, which is described by having a refractive index, when compared with the surrounding medium, of close to unity,  $|m - 1| \ll 1$ , where

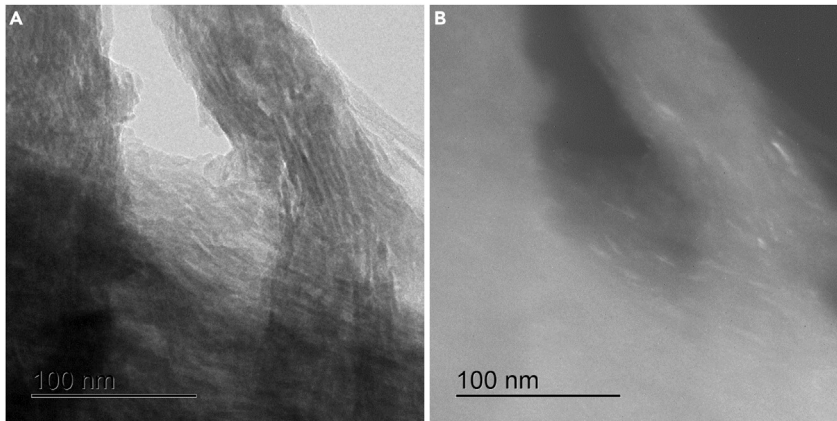


**Figure 5. Comparative TEM to Distinguish between Location of Inorganic and Organic Constituents**

(A) Bright-field TEM showing arrangement of nanorods and (B) dark-field TEM highlighting individual nanorods composed of inorganic material surrounded by an organic matrix.

$m = (n/n_0)$ . Additionally  $x|m - 1| \ll 1$ , where  $x = 2\pi r/\lambda$  must be met. In accordance with RGD, the light-scattering efficiency coefficient  $Q_S^R$ , for randomly oriented nanorods, has been derived by Shapovalov.<sup>33</sup> For a randomly oriented cylinder with a height  $H$  and a radius  $a$ , the light-scattering efficiency coefficient is

$$Q_S^R = \frac{k^4 a^3 H (n^2 - 1)^2}{32\pi^2} \cdot QC(H, a), \quad (\text{Equation 1})$$

where

$$QC(H, a) = \frac{4\pi^2}{3} \left\{ 8 - \frac{22}{45}(kH)^2 - \frac{38}{15}(ka)^2 + \frac{13}{105}(ka)^2(kH)^2 \right\} \quad (\text{Equation 2})$$

and  $k = 2\pi/\lambda$ . The light-scattering efficiency coefficient is determined by dividing the light-scattering cross-section by the cross-sectional area of projection of a particle on a plane and describes how efficiently light can be scattered.<sup>33</sup> In Figure 7,  $Q_S^R$  is plotted against the radius for three different wavelengths (450, 550, and 650 nm),  $H = 20$  nm, and  $n = 1.66$  (the refractive index for HAP). This demonstrates how scattering efficiency decreases as the radius decreases. From TEM micrographs (Figure 4), we conclude that the radius of the nanorods ranges from 0.5 to 1.5 nm and that the height ranges from 5 to 25 nm, which is predicted to produce negligible scattering. Although the RGD is an approximation, it is sufficient to show the scattering dependence on particle size and provides insight into why the teeth are transparent.

### Nanoindentation and the Influence of a Mineralization Density Gradient

The hardness and reduced Young's modulus (mean  $\pm$  SD) of the enamel-like and dentin layers were measured using a nanoindenter (Figure 8). The enamel-like layer is hardest and stiffest with an average hardness of  $4.2 \pm 1.1$  GPa and a reduced modulus of  $43.3 \pm 15.8$  GPa. The hardness is comparable with the teeth of the great white shark and piranha, which are reported as  $4.1 \pm 1.1$  GPa and  $4.1 \pm 0.9$  GPa, respectively.<sup>34</sup> Despite the significant differences in size, morphology, and habitat, the mechanical properties of the enamel-like layer of these predatory species are strikingly similar. The dentin has an average hardness of  $2.1 \pm 1.2$  GPa and a reduced modulus of  $16.4 \pm 7.3$  GPa. When compared with the dentin of the great white shark and piranha, with reported hardnesses of  $0.7 \pm 0.2$  GPa and

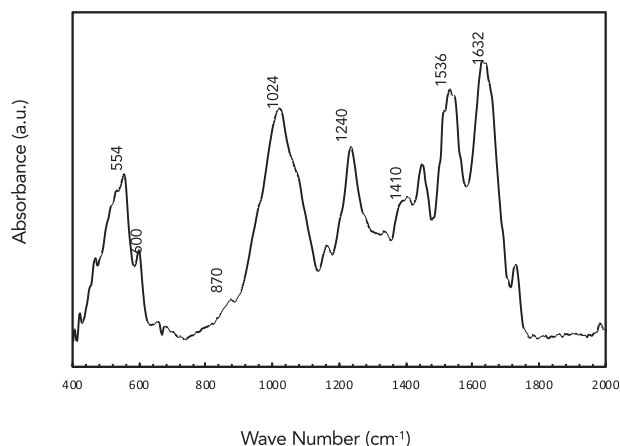


**Figure 6. Fourier Transform Infrared Spectroscopy of a Single Tooth**

Characteristic bands of hydroxyapatite and collagen. Amide I, II, and III bands characteristic of collagen occur at 1,632, 1,536, and 1,240  $\text{cm}^{-1}$ , respectively. Hydroxyapatite bands are:  $\nu_4\text{PO}_4^{3-}$ ,  $\nu_2\text{CO}_3^{2-}$ ,  $\nu_3\text{PO}_4^{3-}$ ,  $\nu_3\text{CO}_3^{2-}$  at 554 and 600, 870, 1,024, and 1,410  $\text{cm}^{-1}$ , respectively. See also Table S1.

0.8  $\pm$  0.3 GPa, respectively, the dragonfish dentin (2.1  $\pm$  1.2 GPa) is much harder, suggesting that it has a higher degree of mineralization and nanoscale structural arrangement, both of which should contribute to transparency.

The teeth are found to have a gradient in mineralization (Figure 8A), which accounts for the variability in hardness with location of indentation. While we report the hardness and reduced modulus as an average value, it is important to note the range. The enamel-like layer was only indented at the tip of the tooth where the surface is large enough to reduce effects from the dentin-enamel junction (DEJ) and the surrounding epoxy. The enamel-like layer has a hardness that ranges from 2.6 to 5.4 GPa while the reduced modulus ranges from 26.8 to 67.9 GPa. The dentin hardness ranges from 0.4 to 3.9 GPa and the reduced modulus ranges from 3.5 to 38.4 GPa.

The degree of mineralization was quantified using thermogravimetric analysis. The resulting value of  $\sim$ 80% mineralization (Figure S6) is indeed greater than the average dentin reported for the teeth of humans with  $\sim$ 75% mineralization, who have tooth hardness similar to that of piranha and great white shark.<sup>35,36</sup> The minimal amount of dispersed collagen fibrils likely reduces scattering. Additionally, the dragonfish teeth lack microscale features such as dentin tubules. Dentin tubules are known to provide energy-absorption properties<sup>37</sup> and inherently reduce the stiffness. The absence of tubules not only accounts for the high stiffness of the dentin layer but also the transparency. The typical coloration of the dentin layer, as seen in human teeth, is associated with scattering that occurs due to the presence of tubules.<sup>38</sup>

## Conclusions

We show that the teeth of dragonfish owe their transparency to a nanoscale structure of hydroxyapatite and collagen, which is devoid of microscale features such as dentin tubules; they are also sufficiently thin ( $\sim$ 60  $\mu\text{m}$ ) to reduce Rayleigh scattering. The enamel-like layer is highly mineralized, consisting of amorphous/nanocrystalline HAP ( $\sim$ 20 nm grain size), while the dentin consists of an array of interpenetrating nanorods ( $\sim$ 5 nm diameter) of HAP embedded within a collagen matrix. This transparency is a unique property that is the result of the nanoscale structure of the teeth, in contrast with the teeth of other animals and humans. Thus, it is an adaptation to

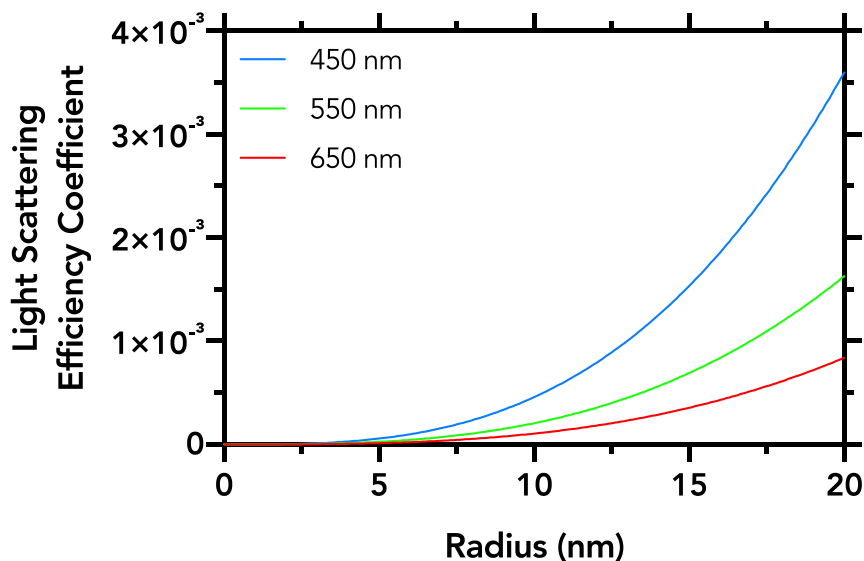


**Figure 7. Light-Scattering Efficiency Coefficient for Randomly Oriented Nanorods versus Radius**

A graph is plotted for three different wavelengths of light (450, 550, and 650 nm). The height of the cylinder was kept constant at 20 nm as the radius varied from 1–20 nm and  $n = 1.66$ .

thriving in the aphotic zone, where biological light (bioluminescence) drives the predator-prey interactions.

The mechanical properties of the enamel-like layer are similar to those of the piranha and the great white shark, despite vast differences in size, morphology, and habitat. However, the dentin, comparatively, is much harder and stiffer with a higher degree of mineralization and a lack of tubules, which is a mechanical trade-off to ensure transparency by reducing scattering. The nanoscale structure also contributes to this higher degree of hardness.

This report is the first to study one species of deep-sea fish, *A. scintillans*, and their transparent teeth. We demonstrated using a variety of characterization techniques that the teeth are extremely hard and sharp, being comparable with those from great white sharks or piranhas. This surprising finding correlates well with the fact that the dragonfish is an efficient predator where food is scarce. In the deep sea, many organisms are able to produce light and use this to navigate around and spot/escape potential prey/predators. Within this context of biological light, the teeth of the dragonfish remain invisible, being built to show no contrast with the surrounding water. Thus, in combination with the blackness of its skin, the array of hard sharp teeth from the dragonfish represents a deadly invisible weapon for an efficient predator.

Our investigation highlights the importance of using the materials science approach to better understand specialized dentition in response to feeding habits, and its usefulness in exploring the ecology of deep-sea organisms and their unknown properties.

## EXPERIMENTAL PROCEDURES

The specimens of *A. scintillans* were collected during the April 29, 2017 SIO research cruise on the ship *R/V Robert Gordon Sproul*, off San Diego in the San Diego Trough. The trough is a deep canyon with an average depth of 1,000 m. Pelagic organisms

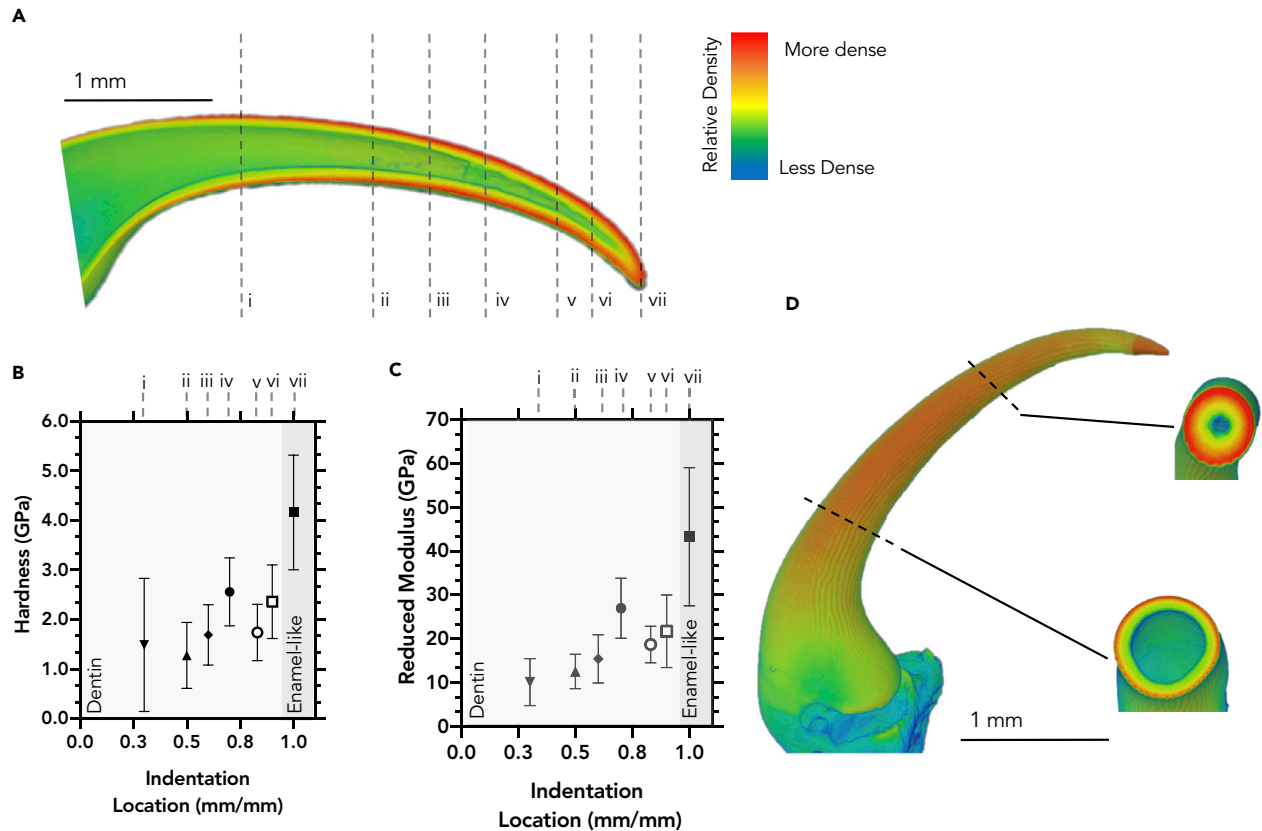


**Figure 8. Influence of Mineralization Gradient on Nanoindentation Location**

(A)  $\mu$ -CT scan of the longitudinal cross-section of a representative tooth. The color mapping indicates relative density signifying degree of mineralization. Hotter colors (red) are more dense while cooler colors (blue) are less dense. There exists a gradient in mineralization that increases from the base toward the tip of the tooth. Roman numerals i–vii mark the relative cross-sections where nanoindentation was performed and align with the designated indentation locations in (B) and (C).

(B) The hardness values (mean  $\pm$  SD) from nanoindentation are dependent on location within the tooth due to the gradient in mineralization as indicated by the  $\mu$ -CT scan.

(C) The reduced modulus values (mean  $\pm$  SD) from nanoindentation are affected by the degree of mineralization.

(D)  $\mu$ -CT scans of transverse cross-sections that indicate the surface in which nanoindentation was performed. The two representative slices demonstrate that the degree of mineralization increases toward the tip of the tooth and outward radially.

The same color mapping was used in (A) and (D).

were collected using mid-water trawling with a net, from a depth of  $\sim$ 500 m. Upon retrieval on the boat deck, organisms were placed directly in cold seawater and sorted for use. Surprisingly, many fishes were still alive and able to survive in a tank for several hours. If (or when) showing no signs of life, the organisms were placed in a  $-20^{\circ}\text{C}$  freezer, or in liquid nitrogen (both available on the ship). Back in the laboratory, the samples were stored in freezers at  $-20^{\circ}\text{C}$  or  $-80^{\circ}\text{C}$  until use.

### Optical Characterization

For optical observation, we defrosted the specimen at laboratory temperature and photographed the fish and teeth under a Nikon SMZ 1500 stereoscope equipped with a Retiga 2000R (QImaging, Surrey, BC, Canada) color digital camera. The system also has an annular ring illumination system to provide omnidirectional lighting, polarizers, and several fluorescence cubes to allow excitation at 355, 390, and 470 nm using an EXFO X-Cite 120 W mercury lamp (long-pass filters were used to visualize the emission). Samples were imaged in air and filtered seawater.

After imaging under the stereoscope, the head was sectioned off the main body using a clean razor blade. The entire head was then either microdissected for “extracting” teeth with minimum flesh attached and analyzed for transparency, or was dehydrated using stepwise increments of increasing ethanol concentration from 40% to 100%. This step was necessary for observation by scanning electron microscopy. Additionally, critical point drying was used to remove excess water and specimens were coated with molybdenum. Fresh specimens were also studied and compared with those that were critically dried to discern between the artifacts from drying. There are no apparent differences between the teeth that were freshly examined and those that were critically dried.

To examine teeth transparency, we used a PARISS hyperspectral imaging system ([www.lightforminc.com](http://www.lightforminc.com)), using teeth separated from the head (see below). The analyses were performed on a Nikon 80i microscope outfitted with a monochrome Retiga 2000DC, CCD camera (QImaging). Wavelength calibration was performed with an MIDL Hg<sup>+</sup>/Ar<sup>+</sup> emission lamp (LightForm, Asheville, NC, USA), and accuracy was recorded and verified to be better than 2 nm. The tip, middle, and base of teeth were mapped for spatial distribution of spectra. The analyses were made in both air and filtered seawater. Air makes them turn less transparent because of changes of refractive index in the air medium (versus water<sup>39</sup>). However, this helped us visualize the spectral distribution in the teeth (translucent rather than transparent). In all cases, 100% of the pixels of the mapped areas showed different ratios of five representative spectra, called “reference spectra.” Distribution of these reference spectra across the pixels of an image was used as a proxy of homogeneity in the sample with regard to letting certain wavelengths pass through the sample. Here, we adopted a minimum correlation coefficient of 98.5% for the analyses, indicating that pixels (or areas of the image) showed the same reference spectrum when having more than 98.5% similarity with the specific reference spectrum. The transmittance and reflectance percentage were calculated by dividing the scan of the tooth by the background. Although five different teeth were analyzed, the data were similar across them, and thus only a representative tooth is presented here for the hyperspectral analysis.

### Microstructural Characterization

More than 40 teeth from ten different specimens were imaged using scanning electron microscopy, and fresh samples were imaged using environmental scanning electron microscopy under a Quanta 400 field-emission gun (FEI, Hillsboro, OR, USA) in low vacuum mode ( $P = 100$  Pa, accelerating voltage 10 kV) equipped with an EDAX Genesis V6.04 (EDAX, Mahwah, NJ, USA) X-ray spectrometer. Specimens for TEM (JEOL JEM-2100 LaB<sub>6</sub> operating at 200 kV accelerating voltage) were either extracted by an FEI Versa3D FIB and post-thinned using a Fischione NanoMill, or prepared by scratching a single tooth on sandpaper and investigating the enamel-like layer. A beam current of 30 pA/cm<sup>2</sup> and a voltage of 30 kV was used.

For X-ray microscopy, an individual tooth was imaged (Xradia 510 Versa; Zeiss, Jena, Germany) with a voxel size of 4.542  $\mu\text{m}$  and an acceleration voltage of 40 kV, resulting in 996 projection images. The images were processed using Amira software (FEI).

### Compositional Analysis

For FTIR, whole teeth were individually used to collect the spectra. The spectra were collected in the absorbance mode in air with  $\sim 25$  N of force applied to the specimen measurement surface using an ATR Spectrum Two instrument (PerkinElmer, Waltham, MA, USA). A background spectrum was first taken for background subtraction using Spectrum 10 software (PerkinElmer). The resultant collected wavelengths were

from  $400\text{ cm}^{-1}$  to  $4,000\text{ cm}^{-1}$  wherein the main mineral and collagen signals were captured. The baseline of each spectrum was corrected using Spectrum 10 software (PerkinElmer).

Thermogravimetric analysis (SDT Q600 Simultaneous TGA/DSC; TA Instruments, New Castle, DE, USA) was used to determine the mineral composition of the dentin. The enamel layer was scraped away using polishing paper to isolate the dentin. On average 15 teeth from more than eight different specimens were used per sample to produce a significant mass ( $\sim 2\text{ mg}$ ) that could be detected by TGA. Samples were then heated from room temperature to  $800^\circ\text{C}$  at a rate of  $10^\circ\text{C}/\text{min}$  under nitrogen. The temperature values to determine each phase composition were used from Vargas-Becerril et al.<sup>35</sup> After  $600^\circ\text{C}$  the water and organic phase is considered to be removed. The mass percentage was calculated by dividing the mass recorded by the initial mass.

### Mechanical Properties

The hardness and reduced modulus of the enamel-like and dentin layers were measured using a nanoindentation testing machine (Nano Hardness Tester; Nano-vea, Irvine, CA, USA) equipped with a Berkovich diamond indenter tip. Five dried teeth from four different specimens were embedded in epoxy and polished perpendicular to the tip to expose the transverse region. These samples were then mounted with superglue onto a steel block with the transverse region exposed. The maximum penetration depth of the indenter tip into the tooth was  $2.67\text{ }\mu\text{m}$ . All indentations were performed by penetrating through each layer with a load of  $15\text{ mN}$ , loading and unloading rates of  $30\text{ mN}/\text{min}$ , and  $20\text{ s}$  of hold time. A total of 5–10 indents were made on each layer and averaged.

### DATA AND SOFTWARE AVAILABILITY

All data needed to evaluate the conclusions in the paper are present in the paper and/or the [Supplemental Information](#). Additional data related to this paper may be requested from the authors.

### SUPPLEMENTAL INFORMATION

Supplemental Information can be found online at <https://doi.org/10.1016/j.matt.2019.05.010>.

### ACKNOWLEDGMENTS

M.A.M. thanks the Humboldt Foundation for granting a research award and the Air Force Office of Research for support under the MURI Program (AFOSR grant no. FA9550-15-0009). Funding from “The Biomimicry for Emerging Science and Technology Initiative” (The BEST Initiative; to D.D.D.) and from the Air Force Office of Scientific Research (AFOSR) grant #FA9550-10-1-0555 (MURI BIOPAINTS) for the hyperspectral imager is acknowledged by D.D.D. This is BEST paper #002. INM support and hospitality to M.A.M. are gratefully acknowledged. We also thank Prof. Jennifer Taylor, SIO/UCSD, for organizing the specimen collection cruise for the SIO125 class (funding provided by UC Ship Funds). Eric Bushong was extremely helpful with X-ray microscopy. Michael Allen is acknowledged for his tremendous help with performing hyperspectral imaging.

### AUTHOR CONTRIBUTIONS

Conceptualization, A.V.-H., D.D.D., E.A., and M.A.M.; Methodology, A.V.-H., D.D.D., M.A.M., and M.K.; Formal Analysis, A.V.-H.; Investigation, A.V.-H., M.K.,

and B.N.; Resources, D.D.D., M.A.M., and E.A.; Writing – Original Draft, A.V.-H., D.D.D., and M.A.M.; Writing – Review & Editing, A.V.-H., D.D.D., E.A., and M.A.M.; Visualization, A.V.-H. and M.A.M.; Supervision, D.D.D. and M.A.M.; Funding Acquisition, D.D.D. and M.A.M.

## DECLARATION OF INTERESTS

The authors declare no competing interests.

Received: January 30, 2019

Revised: April 23, 2019

Accepted: May 8, 2019

Published: June 5, 2019

## REFERENCES

- Meyers, M.A.A., McKittrick, J., and Chen, P.-Y. (2013). Structural biological materials: critical mechanics-materials connections. *Science* 339, 773–779. <http://www.sciencemag.org/content/339/6121/773.full.pdf>.
- Meyers, M.A., Chen, P.-Y., Lopez, M.I., Seki, Y., and Lin, A.Y.M. (2011). Biological materials: a materials science approach. *J. Mech. Behav. Biomed. Mater.* 4, 626–657. <http://www.ncbi.nlm.nih.gov/pubmed/21565713>.
- Meyers, M.A., Chen, P.-Y., Lin, A.Y.-M., and Seki, Y. (2008). Biological materials: structure and mechanical properties. *Prog. Mater. Sci.* 53, 1–206.
- Chen, P.-Y., McKittrick, J., and Meyers, M.A.A. (2012). Biological materials: functional adaptations and bioinspired designs. *Prog. Mater. Sci.* 57, 1492–1704.
- Naleway, S.E., Taylor, J.R.A., Porter, M.M., Meyers, M.A., and McKittrick, J. (2016). Structure and mechanical properties of selected protective systems in marine organisms. *Mater. Sci. Eng. C Mater. Biol. Appl.* 59, 1143–1167. <http://www.sciencedirect.com/science/article/pii/S092849311530463X>.
- Haddock, S.H.D., Moline, M.A., and Case, J.F. (2010). Bioluminescence in the sea. *Ann. Rev. Mar. Sci.* 2, 443–493. <http://www.annualreviews.org/doi/10.1146/annurev-marine-120308-081028>.
- Bakes, M.J., Elliott, N.G., Green, G.J., and Nichols, P.D. (1995). Variation in lipid composition of some deep-sea fish (Teleostei: Oreosomatidae and Trachichthyidae). *Comp. Biochem. Physiol. B Biochem.* 111, 633–642.
- Neighbors, M.A., and Nafpaktitis, B.G. (1982). Lipid compositions, water contents, swimbladder morphologies and buoyancies of nineteen species of midwater fishes (18 myctophids and 1 neoscopelid). *Mar. Biol.* 66, 207–215.
- Clarke, T.A. (1982). Feeding habits of stomioid fishes from Hawaiian waters. *Fish. Bull.* 80, 287–304.
- Hopkins, T.L. (1996). Trophic ecology of the stomiid (Pisces: Stomiidae) fish assemblage of the eastern Gulf of Mexico: strategies, selectivity and impact of a top mesopelagic predator group. *Mar. Biol.* 127, 179–192.
- Kenaley, C.P. (2012). Exploring feeding behaviour in deep-sea dragonfishes (Teleostei: Stomiidae): jaw biomechanics and functional significance of a loosejaw. *Biol. J. Linn. Soc.* 106, 224–240.
- Li, L., and Ortiz, C. (2013). Biological design for simultaneous optical transparency and mechanical robustness in the shell of placuna placenta. *Adv. Mater.* 25, 2344–2350.
- Carter, J.G., and Schneider, J.A. (1997). Condensing lenses and shell microstructure in *Corculum* (Mollusca: Bivalvia). *J. Paleontol.* 71, 56–61.
- Johnsen, S., and Widder, E.A. (1998). Transparency and visibility of gelatinous zooplankton from the Northwestern Atlantic and Gulf of Mexico. *Biol. Bull.* 195, 337–348.
- Mensingher, A.F., and Case, J.F. (1990). Luminescent properties of deep sea fish. *J. Exp. Mar. Bio. Ecol.* 144, 1–15.
- Douglas, R.H., Partridge, J.C., Dulai, K.S., Hunt, D.M., Mullineaux, C.W., and Hynninen, P.H. (1999). Enhanced retinal longwave sensitivity using a chlorophyll-derived photosensitizer in *Malacosteus niger*, a deep-sea dragon fish with far red bioluminescence. *Vis. Res.* 39, 2817–2832.
- Hunt, D.M., Dulai, K.S., Partridge, J.C., Cottrill, P., and Bowmaker, J.K. (2001). The molecular basis for spectral tuning of rod visual pigments in deep-sea fish. *J. Exp. Biol.* 204, 3333–3344.
- Gregory, W.K. (1933). *Fish Skulls: A Study of the Evolution of Natural Mechanisms* (American Philosophical Society).
- Shellis, R.P., and Berkovitz, B.K.B. (1976). Observations on the dental anatomy of piranhas (Characidae) with special reference to tooth structure. *J. Zool.* 180, 69–84.
- Hainsworth, S.V., Delaney, R.J., and Rutty, G.N. (2008). How sharp is sharp? Towards quantification of the sharpness and penetration ability of kitchen knives used in stabbings. *Int. J. Legal Med.* 122, 281–291.
- Mahamid, J., Sharir, A., Addadi, L., and Weiner, S. (2008). Amorphous calcium phosphate is a major component of the forming fin bones of zebrafish: Indications for an amorphous precursor phase. *Proc. Nat. Acad. Sci. U S A* 105, 12748–12753. <http://www.pnas.org/cgi/doi/10.1073/pnas.0803354105> <http://www.ncbi.nlm.nih.gov/pubmed/18753619>.
- Benedict, H.C. (1928). A note on the fluorescence of teeth in ultra-violet rays. *Science* 67, 442. <http://www.sciencemag.org/cgi/doi/10.1126/science.67.1739.442>.
- Horsley, H.J. (1967). Isolation of fluorescent material present in calcified tissues. *J. Dent. Res.* 46, 106.
- McDevitt, C.A., and Armstrong, W.G. (1969). Investigation into the nature of the fluorescent material in calcified tissues. *J. Dent. Res.* 48, 1108.
- Winter, R. (1993). Visualizing the natural dentition. *J. Esthet. Restor. Dent.* 5, 103–118.
- Matsumoto, H., Kitamura, S., and Araki, T. (2001). Applications of fluorescence microscopy to studies of dental hard tissue. *Front. Med. Biol. Eng.* 10, 269–284. <http://www.ncbi.nlm.nih.gov/pubmed/11334168>.
- Lee, Y.-K. (2015). Fluorescence properties of human teeth and dental calculus for clinical applications. *J. Biomed. Opt.* 20, 040901. <http://biomedicaloptics.spiedigitallibrary.org/article.aspx?doi=10.1117/1.JBO.20.4.040901>.
- de Wolff, P.M. (1968). A simplified criterion for the reliability of a powder pattern indexing. *J. Appl. Crystallogr.* 1, 108–113. <http://scripts.iucr.org/cgi-bin/paper?S002188986800508X>.
- Lopes, C.de C.A., Limirio, P.H.J.O., Novais, V.R., and Dechichi, P. (2018). Fourier transform infrared spectroscopy (FTIR) application chemical characterization of enamel, dentin and bone. *Appl. Spectrosc. Rev.* 53, 747–769.
- Figueiredo, M.M., Gamelas, J.A.F., and Martins, A.G. (2012). Characterization of bone and bone-based graft materials using FTIR spectroscopy. In *Infrared Spectroscopy—Life and Biomedical Sciences*, T. Theophile, ed. (IntechOpen). <http://www.intechopen.com/books/infrared-spectroscopy-life-and-biomedical-sciences/characterization-of-bone-and-bone-based-graft-materials-using-ftir-spectroscopy>.
- Bachmann, L., Diebolder, R., Hibst, R., and Zzell, D.M. (2003). Infrared absorption

- bands of enamel and dentin tissues from human and bovine teeth. *Appl. Spectrosc. Rev.* 38, 1–14.
32. Wyatt, P.J. (2014). Measurement of special nanoparticle structures by light scattering. *Anal. Chem.* 86, 7171–7183.
  33. Shapovalov, K.A. (2004). Light scattering of cylindrical particles in Rayleigh- Gans-Debye approximation. 2. Randomly oriented particles. *Atmos. Ocean Opt.* 17, 627–629.
  34. Chen, P.-Y., Schirer, J., Simpson, A., Nay, R., Lin, Y.-S., Yang, W., Lopez, M.I., Li, J., Olevsky, E.A., and Meyers, M.A. (2012). Predation versus protection: fish teeth and scales evaluated by nanoindentation. *J. Mater. Res.* 27, 100–112. [http://www.journals.cambridge.org/abstract\\_S0884291411003323](http://www.journals.cambridge.org/abstract_S0884291411003323).
  35. Vargas-Becerril, N., García-García, R., and Reyes-Gasga, J. (2018). Structural changes in human teeth after heating up to 1200°C in argon atmosphere. *Mater. Sci. Appl.* 9, <https://doi.org/10.4236/msa.2018.97046>.
  36. Marshall, G.W., Balooch, M., Gallagher, R.R., Gansky, S.A., and Marshall, S.J. (2001). Mechanical properties of the dentinoenamel junction: AFM studies of nanohardness, elastic modulus, and fracture. *J. Biomed. Mater. Res.* 54, 87–95.
  37. McKittrick, J., Chen, P.Y., Tombolato, L., Novitskaya, E.E., Trim, M.W., Hirata, G.A., Olevsky, E.A., Horstemeyer, M.F., and Meyers, M.A. (2010). Energy absorbent natural materials and bioinspired design strategies: a review. *Mater. Sci. Eng. C* 30, 331–342.
  38. Zijp, J.R., and ten Bosch, J.J. (2009). Theoretical model for the scattering of light by dentin and comparison with measurements. *Appl. Opt.* 32, 411–415.
  39. Bagge, L.E., Osborn, K.J., and Johnsen, S. (2016). Nanostructures and monolayers of spheres reduce surface reflections in hyperiid amphipods. *Curr. Biol.* 26, 3071–3076.

**Matter, Volume 1**

**Supplemental Information**

**On the Nature of the Transparent**

**Teeth of the Deep-Sea**

**Dragonfish, *Aristostomias scintillans***

**Audrey Velasco-Hogan, Dimitri D. Deheyn, Marcus Koch, Birgit Nothdurft, Eduard Arzt, and Marc A. Meyers**

## Supplementary Materials

**Table S1. Fourier-transform infrared spectroscopy absorption bands for a tooth sample and their functional groups**

Wave number (cm <sup>-1</sup> )	Assignment	Reference
554, 600	$\nu_4\text{PO}_4^{3-}$	30
870	$\nu_2\text{CO}_3^{2-}$ ,	30
1024	$\nu_3\text{PO}_4^{3-}$ ,	30
1240	Amide III	28
1410	$\nu_3\text{CO}_3^{2-}$	30
1536	Amide II	28
1632	Amide I	28,29

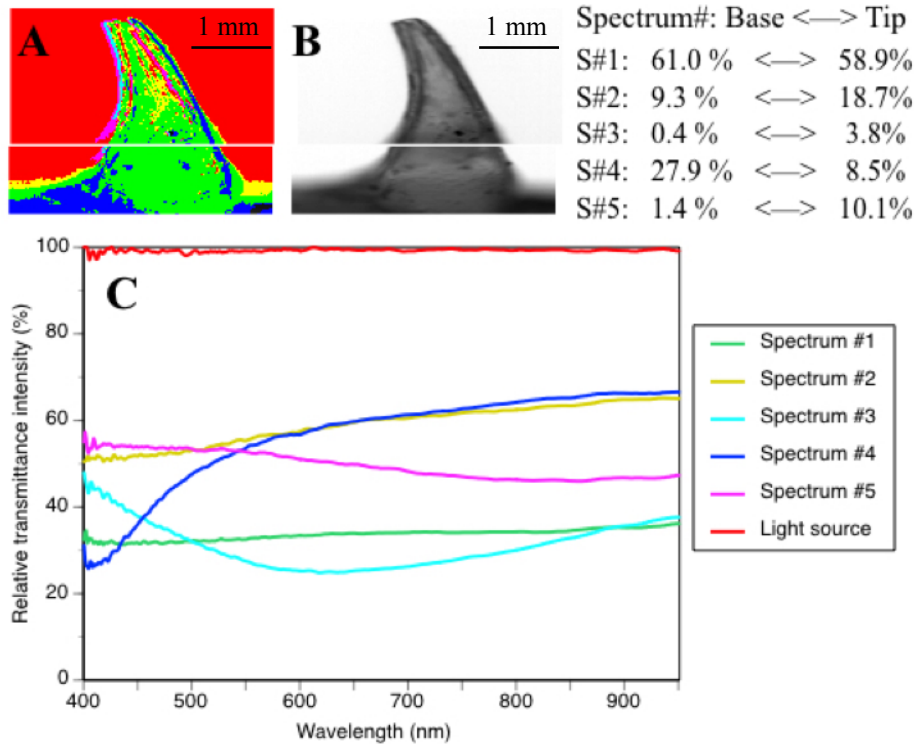


**Figure S1. Hyperspectral analysis in transmittance of one air-dried tooth. (A)** Map showing spatial distribution of the five spectra color-coded differently (note that the tooth is still fully transparent in some areas, as shown by the red-coded spectrum identical to the light source) **(B)** Grey-scale image of the tooth indicating its relative intensity of translucency. **(C)** The five reference spectra color-coded, and the light source spectrum (outside the sample area). Percent of pixel occurrence for each spectrum is given for the base and the tip of the tooth.

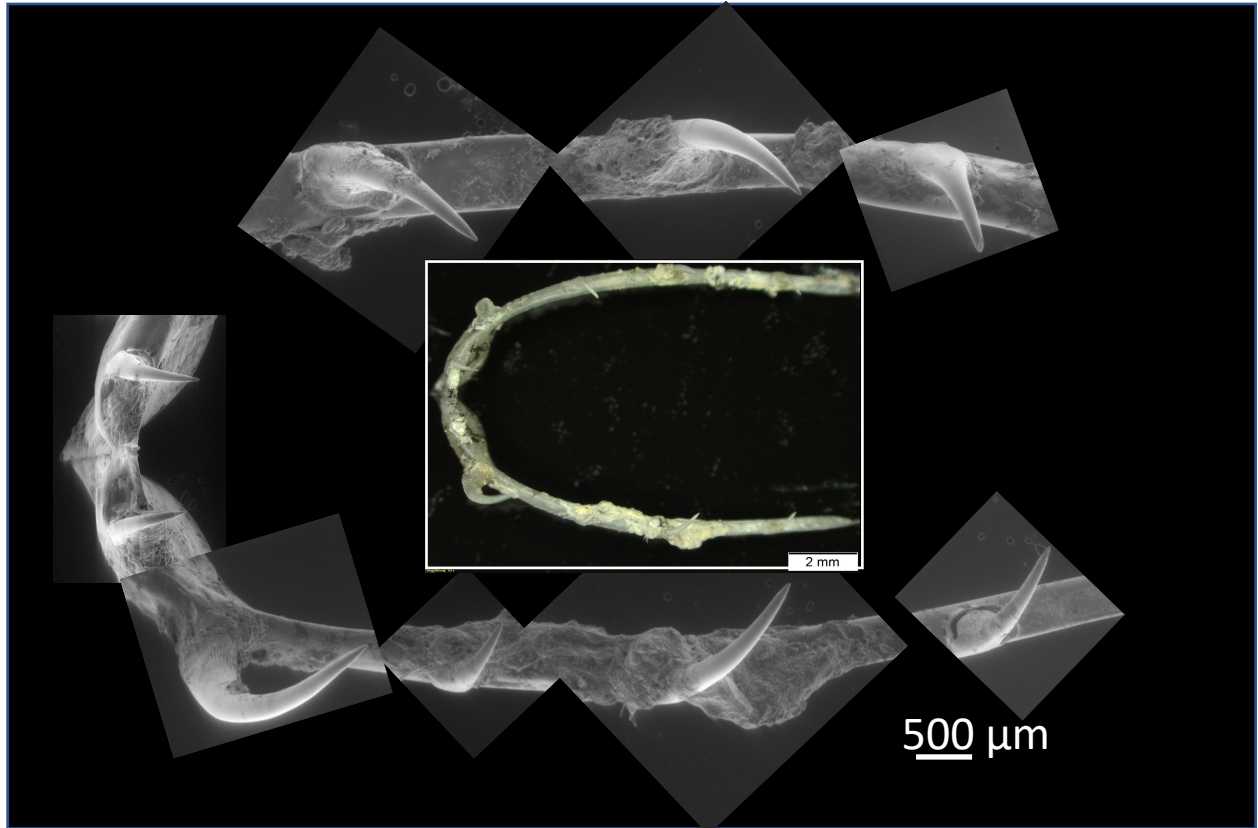


**Figure S2. Fresh sample of a dissected jaw with each tooth characterized by ESEM.** Orientation and location of the teeth in the jaw is shown. The concave surface is striated while the more exposed surface is smooth.

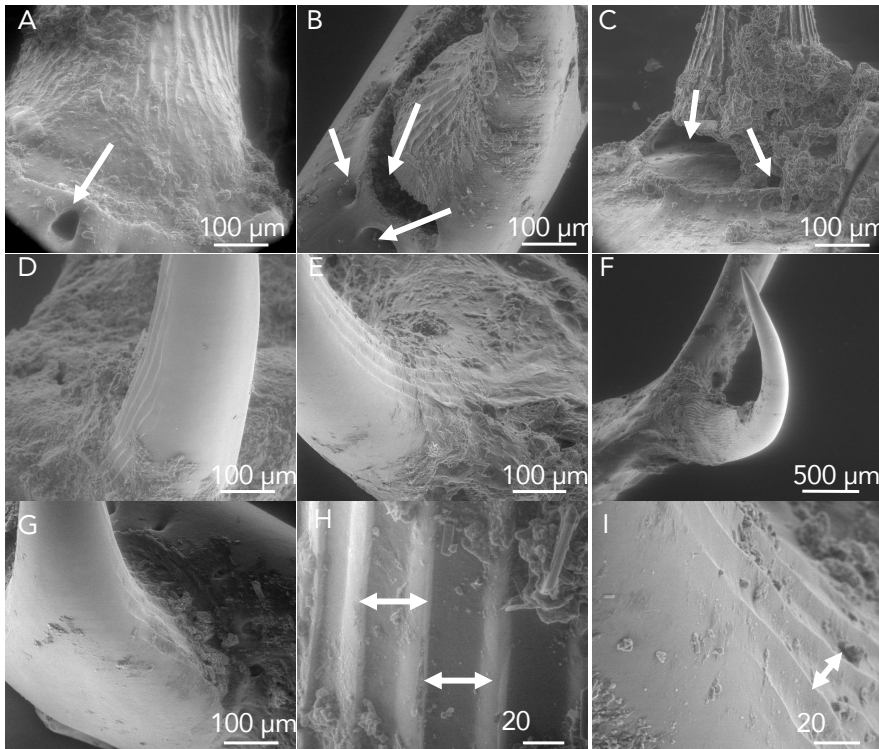


**Figure S3. Details of the concave side of representative teeth showing longitudinal striations.**

Teeth imaged in Figure S2. (A-C) Note perforation in bottom of teeth marked with arrows; (D-G) different teeth; (H,I): detailed view of ridges that are  $\sim 20 \mu\text{m}$  apart and have a radius of curvature, at the apex, of approximately  $1\text{-}2 \mu\text{m}$ .

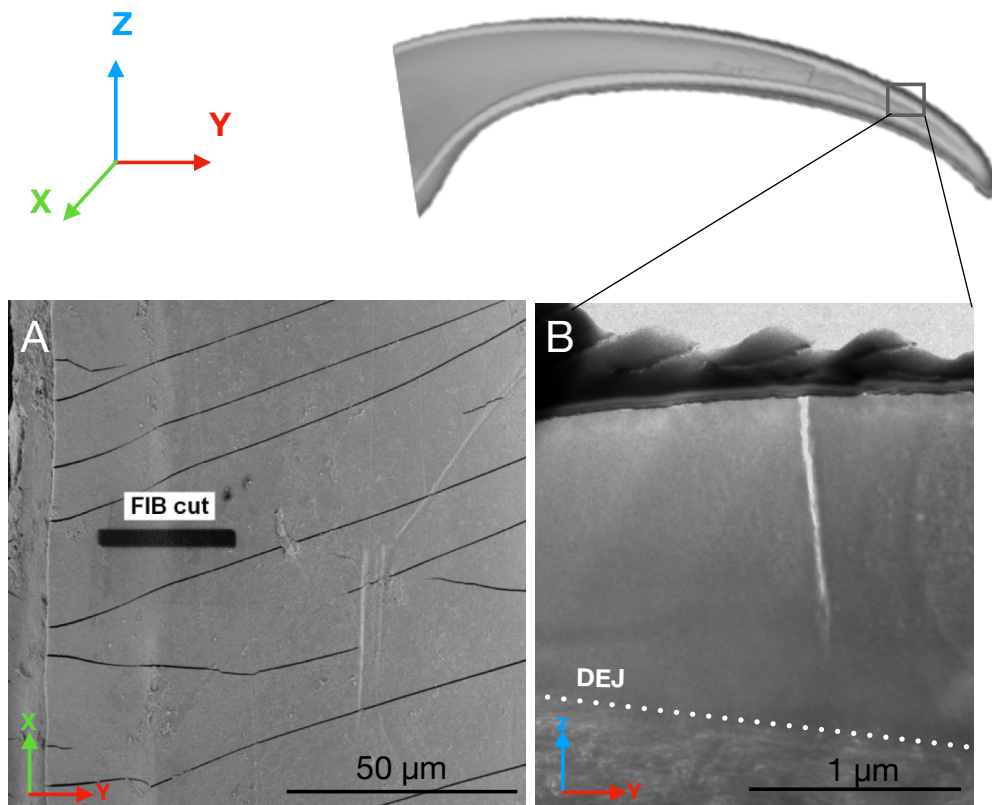


**Figure S4. Crack formation and propagation.** (A) Pattern of circumferential cracks in the enamel-like layer and FIB sample removal. (B) TEM showing crack initiating from the fracture surface and propagating through the enamel-like layer and arresting before the dentin.

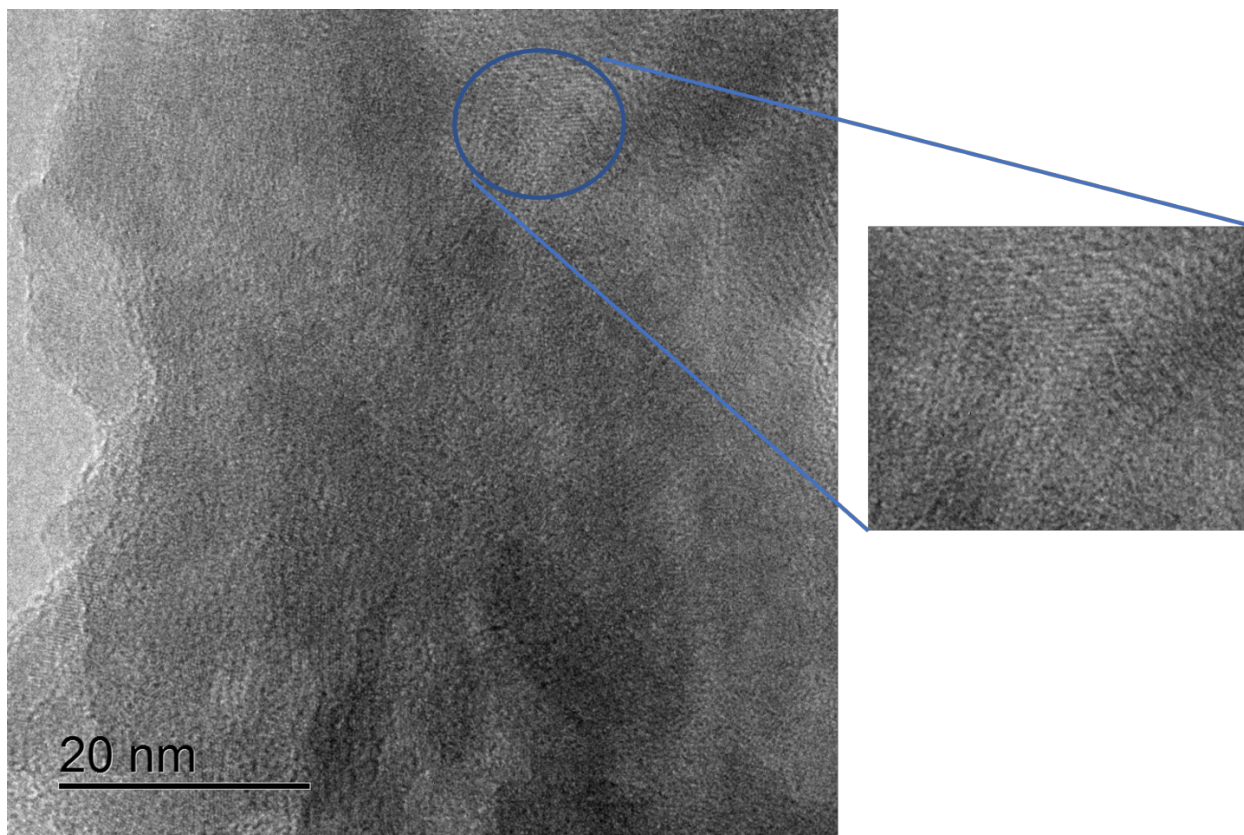


**Figure S5. Transmission electron micrograph of enamel-like region showing amorphous matrix and nanocrystalline domains (Moiré pattern of region circled).** This sample was prepared by a unique procedure not using FIB. This is shown to compare sample preparations. The enamel-like layer of the tooth was rubbed against sandpaper to detach fragments. The fragments were floated in water and placed on a 3 mm copper grid covered with amorphous carbon. These fragments were imaged and shown here. Ultimately, the different sample preparations yielded similar results which show an amorphous matrix with nanocrystalline domains.

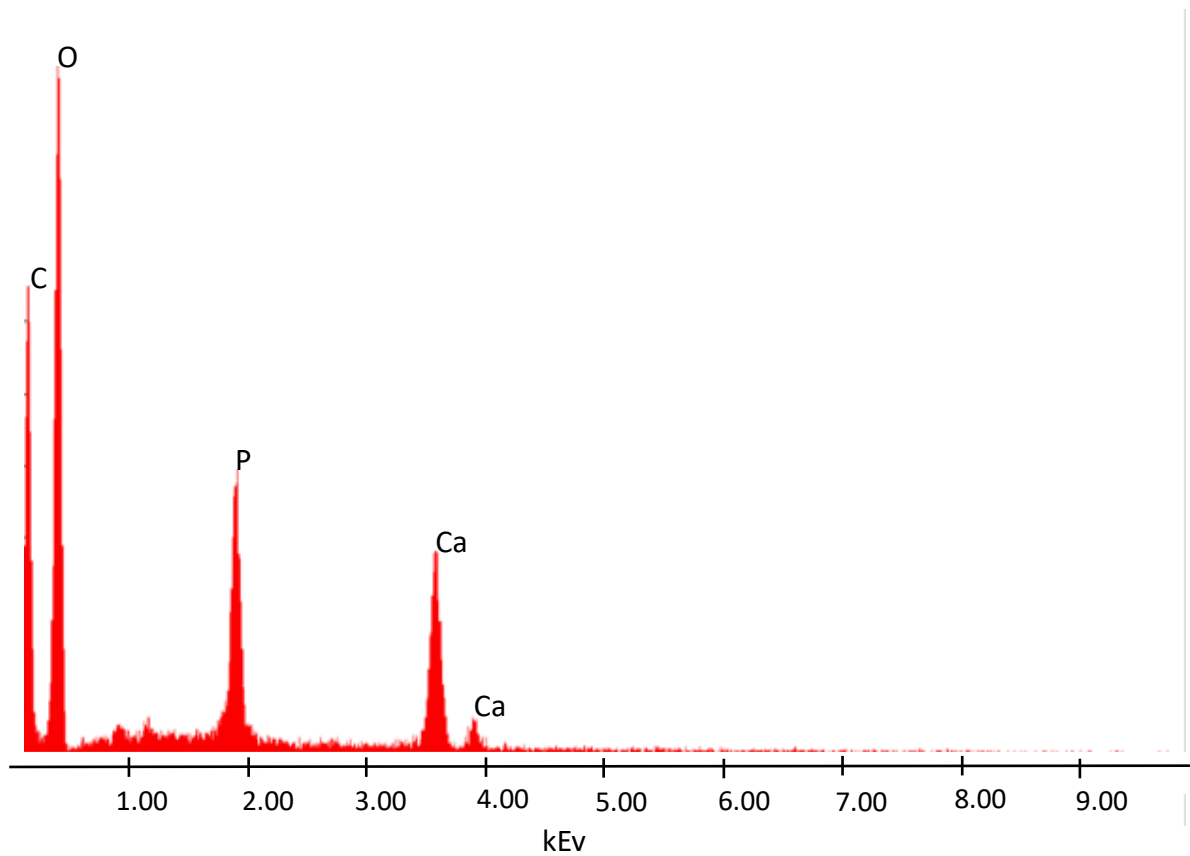


**Figure S6. EDX composition scans of a single tooth.** This shows presence of carbon, oxygen, phosphorous, and calcium which are all constituents of HAP and collagen.

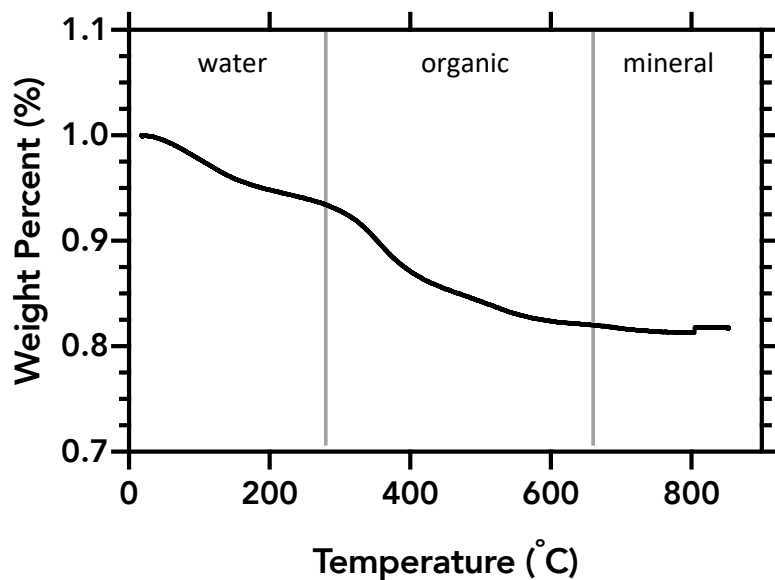


**Figure S7. Thermogravimetric analysis of dentin.** This shows the relative composition of dentin (water, organic, and mineral). The removal of water and organic happens after 600°C. The relative weight percent of water, organic, and mineral is roughly 7%, 12%, and 81% respectively.